Nano Energy 46 (2018) 91–100

Contents lists available at ScienceDirect

Nano Energy

journal homepage: www.elsevier.com/locate/nanoen

Full paper

Structure-property relationships at Nafion thin-film interfaces: Thickness effects on hydration and anisotropic ion transport

Steven C. DeCaluwe[a,b,*], Andrew M. Baker[b,1], Pavan Bhargava[b,2], John E. Fischer[a], Joseph A. Dura[b]

[a] Department of Mechanical Engineering, Colorado School of Mines, Golden, CO 80401, USA
[b] NIST Center for Neutron Research, Gaithersburg, MD 20899, USA

ARTICLE INFO

Keywords:
Nafion
Lamellae
Confinement
PEM fuel cell
Neutron reflectometry
Ionic conductivity

ABSTRACT

The effect of film thickness on water uptake and structure in ultra-thin Nafion is probed via in situ neutron reflectometry for a series of 10 films with thicknesses ranging from 5 to 153 nm. Observed interfacial lamellae are used to understand anomalous transport limitations in such films. Results show three distinct thickness regimes: (*i*) in the truncated regime (< 12 nm), the entire film consists of lamellae; (*ii*) in the thin-film regime (12–42 nm), a non-lamellar bulk-like layer forms between the lamellae and vapor; (*iii*) in the thick-film regime (≥ 60 nm), the bulk-like layer thickness exceeds the radius of gyration for thin-film Nafion. The water uptake in the sample varies non-monotonically with thickness, and can be ordered as: thin-film < truncated < thick-film. In the thin-film regime, the water uptake in the bulk-like layer and lamellae are equal, and both increase with thickness, except for a well-hydrated layer adjacent to the SiO_2 substrate. In the thick-film regime, the bulk-like layer water uptake equals that in macroscopic Nafion membranes, and is invariant with film thickness, while the lamellar water uptake greatly exceeds this. Composition depth profiles are used to predict the anisotropic ionic conductivities. These are fitted to previously published experimental results to demonstrate that the lamellar structure is required for accurate conductivity predictions. These results provide key insights for minimizing transport losses in fuel cell catalyst layers.

1. Introduction

Due to its high ionic conductivity and chemo-thermo-mechanical stability, Nafion[3] is the state-of-the-art polymer electrolyte material for a range of electrochemical energy and separation devices, including polymer electrolyte membrane fuel cells (PEMFCs) [1–8], batteries [9–12], water electrolyzers [13–16], and chemical sensors [17–21]. Nafion's properties depend on the phase segregation between its two primary moieties: the hydrophobic Teflon-like backbone and the hydrophilic sulfonic-acid-terminated side chain. This segregation is highly sensitive to Nafion's thermo-chemical environment and material interfaces. Durable and efficient electrochemical devices, including PEMFCs and “beyond Li-ion” batteries such as Li-sulfur [22–26] and Li-O_2 [27–31], therefore require understanding and control of Nafion's structural and functional properties. Such advances will also yield important insights for a broad class of related ionic copolymers.

For PEMFCs, much attention has focused on the polymer structure and structure-property relationships in bulk membranes [32–52]. Several models of the Nafion ionic domain morphology as a function of hydration have been fit to small angle scattering data. These include water-rich clusters [53] that evolve into filaments at higher humidity [52,54], water cylinders in a polymer matrix [46], or lamellae [51,55]. The inverse has also been proposed, with elongated polymer aggregates that bundle [49], possibly into ribbon-like units [50]. Real space probes of Nafion morphology show that the water-rich domains are a three-dimensionally connected wire-like [48] or ribbon-like [32] network.

Only recently has attention turned to Nafion properties in the catalyst layer (CL), the heterogeneous region where limiting charge-transfer processes occur in PEMFCs (Fig. 1a). Recent work suggests that high transport resistance in CL Nafion contributes to poor PEMFC performance with low Pt loading [5,56–59], but the specific causes of these limitations are not fully understood [58–60]. Understanding is

* Corresponding author at: Department of Mechanical Engineering, Colorado School of Mines, Golden, CO 80401, USA.
E-mail address: decaluwe@mines.edu (S.C. DeCaluwe).
[1] Present address: Los Alamos National Laboratory, Los Alamos, NM 87545, USA.
[2] Present address: Department of Electrical Engineering and Computer Science, University of California, Berkeley, CA 94720, USA.
[3] Certain commercial equipment, instruments, materials, suppliers, or software are identified in this paper to foster understanding. Such identification does not imply recommendation or endorsement by the National Institute of Standards and Technology, nor does it imply that the materials or equipment identified are necessarily the best available for the purpose.

https://doi.org/10.1016/j.nanoen.2018.01.008
Received 24 September 2017; Received in revised form 29 November 2017; Accepted 2 January 2018

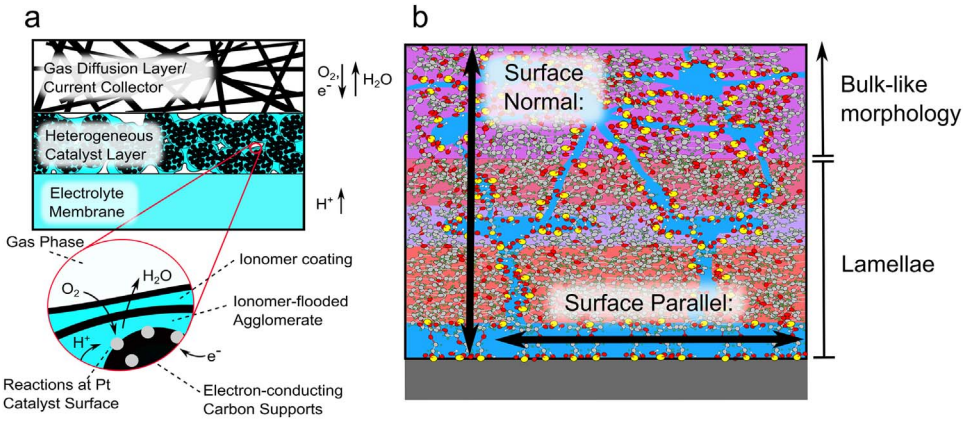

Fig. 1. Illustration of PEMFC processes and structure. (a) Illustration of limiting processes associated with the PEMFC catalyst layer agglomerates, as highlighted in the call-out. (b) Schematic illustration of Nafion thin-film structure at a hydrophilic interface, including the sheet-like lamellae and well-mixed, bulk-like outer layer. Effective proton conductivities in this work are calculated in both the 'surface normal' and 'surface parallel' directions.

hindered by the complex CL nano-structure, where thin Nafion layers coat ionomer-flooded agglomerates of carbon-supported Pt catalyst nanoparticles, and by the complex influence of multiple material interfaces and operating conditions on the thin-film Nafion properties.

For these reasons, researchers increasingly use planar thin-films as a model system to obtain fundamental insight into CL Nafion properties. Results show deleterious changes in stiffness [61], water uptake and mobility [1,57,62–67], and conductivity [5,6,56,59,67–69] with decreasing film thickness below ca. 60 nm. Studies also show that water uptake is influenced by substrate interfaces [1,57,63], thermal processing [56,59] and deposition method [57]. Some have observed an increase in water uptake for films thinner than roughly 20 nm, compared to those between 20 and 60 nm [57,58]. These studies provide valuable insights into thin-film Nafion, but the majority of them report the average sample properties. Because transport is driven by *local* gradients in species free energy and is closely tied to Nafion structure, in situ depth-profiles are required to correlate thin-film Nafion structure with the resulting transport properties.

We report here the thickness dependence of water uptake, interfacial ionic domain structure, and anisotropic ionic conductivity in ultrathin Nafion films (5–153 nm) on SiO_2 substrates, probed via in situ neutron reflectometry (NR). Reflectometry is a highly sensitive probe of planar structures in thin-films [70,71], and NR has been incredibly useful for probing Nafion—substrate interfaces [62–65,72,73]. Hydrophilic substrates such as SiO_2 have been discovered [63] to induce alternating water-rich and water-poor lamellae (i.e. extended planar features) at the Nafion-substrate interface [62–65] followed by a bulk-like layer of Nafion (Fig. 1b). Previously, we used NR to quantify the phase segregation of Nafion moieties in these lamellae, and confirm that they are formed due to interactions between the side chain-terminating SO_3H groups and the SiO_2 substrate [64].

Results herein show that the water uptake in the bulk-like layer increases with increasing thickness for films with equivalent Nafion thickness $t_{Naf} < 60$ nm, but above 60 nm these layers have constant water uptake, similar to bulk 1100 equivalent weight (EW) Nafion ($\lambda = 10$). While the lamellae form due to substrate interactions, their structure and water uptake are influenced by the presence and water uptake of the bulk-like layer. Results also indicate that whole-sample averages represent an insufficient measure for inferring the Nafion water uptake. Calculating effective ionic conductivities for Nafion thin-films from the NR profiles demonstrates how the Nafion thickness, interfacial morphology, and water uptake influence conductivity in the PEMFC CL.

Several factors motivate the use of the SiO_2 substrate here, rather than the technologically relevant Pt substrate: (*i*) the transport measurements against which we fit our conductivity models were done on SiO_2 substrates (presumably to reduce the effects of a conducting Pt layer on those measurements); (*ii*) Nafion forms similar structures on Pt substrates, but with fewer lamellae [72–75]. Therefore, greater sensitivity to the lamellae is achieved in the multi-lamellar system on SiO_2, which may yield insights into similar (but less easily measured) structures on Pt; (*iii*) measurement on SiO_2 allows facile comparison to the many previous studies with SiO_2 substrates [45,56,57,59,62–64,68,76,77]; and (*iv*) previous NR work demonstrates that Nafion interfacial lamellae are promoted both by substrate hydrophilicity and by specific chemical interactions [63,65]. Chemical treatments to improve Pt dispersion and PEMFC CL durability may therefore generate multi-lamellar Nafion structures [75,78–80]. Additional studies will be required to extend these results to a broader range of substrates.

2. Materials and methods

2.1. Sample fabrication and NR measurement

A detailed explanation of the NR data collection and fitting process is given in our previous publication [64], but briefly: Nafion thinfilms, ranging from thickness from 5 nm to 153 nm, were deposited onto 5 mm thick, polished Si wafers (with native SiO_2 intact). The Si wafers were cleaned via detergent scrub and UV-ozone treatment prior to Nafion deposition, and Nafion films were deposited via spin coating, from a commercial dispersion diluted with HPLC-grade ethanol. The concentration of the dispersion and, in some cases, the spin speed were varied to control the resulting Nafion film thickness. Full details of the spin-coat recipes are provided in the Supporting information. Samples were subsequently heated for ≥ 1 h at 60 °C under vacuum to ensure solvent removal, adhesion to the substrate, and consistent thermal history. After fabrication, wafers were installed in the controlled RH chamber, as described previously [64], and NR was measured under 92.1 ± 1.5% RH and at $T = 29.6 \pm 0.2$ °C, with dry Ar vapor humidified by H_2O. Error bars and uncertainties throughout the manuscript represent plus or minus one standard deviation. For select samples, NR was also measured under 92.0% RH humidified by D_2O and/or under 0% RH (dry Ar vapor).

2.2. NR fitting

NR measures the intensity of a reflected neutron beam as a function of grazing angle from the surface. Fitting NR data determines the 1-D depth profile (averaged in the plane of the film) of the scattering length density (SLD), which is the linear combination of the known bound coherent scattering lengths b_k [nm] of all isotopes k in the layer, multiplied by their number density n_k [1/nm^3]:

$$SLD = \sum_k b_k n_k. \quad (1)$$

Unlike x-ray or electron probes, the neutron SLD can be relatively sensitive to light elements, and b_k varies greatly with the isotopes of

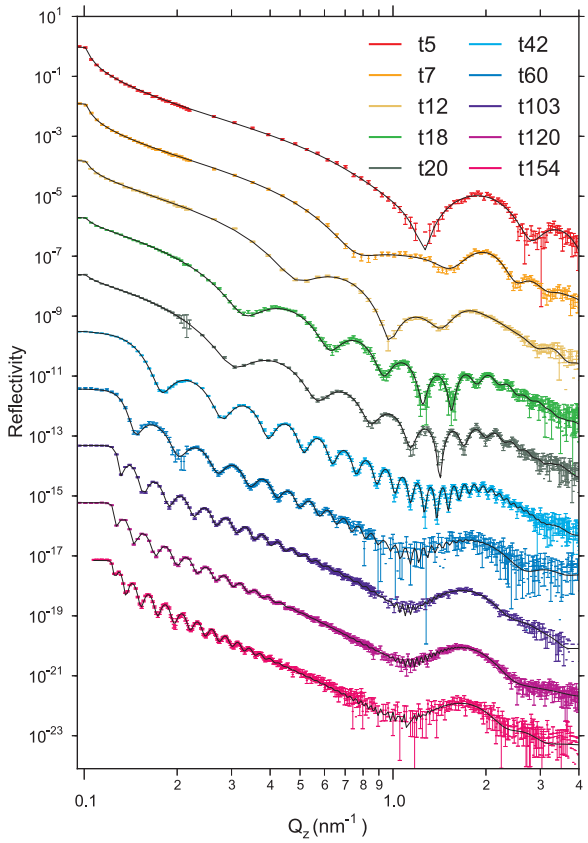

Fig. 2. Reflectivity data (symbols) and best fits (black lines) for Nafion thin-films with equivalent Nafion thicknesses ranging from 5 nm ≤ t_{Naf} ≤ 154 nm. Error bars represent ± 1 standard deviation. Reflectivity curves are offset, with respect to the y-axis, for ease of visualization.

certain elements. In particular, the large SLD contrast between water (SLD_{H2O} = −5.6 ×10^{-5} nm^{-2}) and dry Nafion (SLD_{Nafion} = 4.16 ×10^{-4} nm^{-2}) and between H_2O and D_2O (SLD_{D2O} = 6.36×10^{-4}nm^{-2}) allows for precise, accurate determination of the water concentration profile in Nafion.

In this study, humidified Nafion is modeled as a mixture of water and dried Nafion, where the SLD of the two-phase mixture at any given depth z is equal to a linear combination of the individual phase SLDs, weighted by their volume fractions:

$$SLD(z) = V_{water}(z)SLD_{water} + (1 - V_{water}(z))SLD_{Nafion}. \quad (2)$$

$(1-V_{water}(z))$ is used because the volume fractions of the two phases sum to one. In this manner, the SLD profile fitted to the NR data provides the water V_{water} depth profile.

All sample names here take the form 'tXX', where the number XX is the sample's equivalent Nafion thickness, t_{Naf}, i.e. the resulting thickness if all water were removed:

$$t_{Naf} = \sum_i (1 - V_{water,i})t_i, \quad (3)$$

where t_i is the thickness and $V_{water,i}$ is the water volume fraction of layer i, summed over all i layers in the model. For example, a sample with t_{Naf} = 50 nm is named 't50.'

NR data were fit using Refl1D [70,81], with the SLD profile modeled as a series of layers with finite thickness, interfacial width, and SLD. To allow for the higher SLDs associated with Nafion moiety phase segregation near the SiO_2 interface [64], the water volume fraction V_{water} for any given layer was allowed to vary between −25% and 100%. Non-physical values (V_{water} < 0) are allowed during fitting to accurately match the SLD profile, but are replaced during analysis, as indicated below, with equivalent physical composition profiles [63]. To reduce the number of fitting parameters and eliminate those for which NR results showed limited sensitivity, the interfacial width at the Nafion-SiO_2 interface was set equal to either the value at the Si-SiO_2 interface or that of the inter-lamellar interfaces. For all samples, reduced χ^2 ≤ 1.26 were obtained, signifying excellent fits. In cases where multiple models provided suitable fits to the NR data, the Bayesian Information Criterion was used to discriminate between models [64,82]. For two samples (t103 and t120), an additional layer at the Nafion/vapor interface, roughly 3 nm thick, was required, as discussed below. For samples where NR was collected at both 92% and 0% RH, fits were constrained such that t_{Naf} was equal in both fits (i.e. water uptake values determined from layer SLD analysis and from swelling are equivalent).

2.3. Estimating transport properties in thin-film Nafion and lamellae

Estimating the transport properties of CL Nafion remains a challenge, due to the complex microstructure of the CL and to a limited number of direct transport measurements in thin-film Nafion for predictive modeling capabilities. To provide a first-order approximation of transport parameters in CL Nafion, a few basic assumptions are made. Because there have been no studies, to our knowledge, which calculate transport properties in Nafion interfacial lamellae as a function of water uptake or ionic domain structure, our *a priori* assumption is that the local ionic conductivity for thin-film Nafion obeys the dependence on λ that has been previously-determined for bulk-like samples [43,83]:

$$\sigma_{io} = (0.5139\,\lambda - 0.326)\exp\left(1268\left(\frac{1}{303} - \frac{1}{T}\right)\right), \quad (4)$$

where T is the temperature (302.75 K, here) and λ is the molar ratio of water to sulfonic acid. For "well mixed" Nafion (where the phase segregation is isotropic in nature), this is a function of the local water content:

$$\lambda = \frac{V_{water}}{1-V_{water}}\frac{\rho_{H2O}}{\rho_{Nafion}}\frac{EW_{Nafion}}{MW_{H2O}}, \quad (5)$$

where ρ_m is the mass density of phase m (g/cm^3), EW_{Nafion} is the polymer mass per mole of sulfonate (1100 g/mol in this study), and MW_{H2O} is the molecular weight of water (g/mol). In bulk Nafion, isotropic phase segregation implies a constant ratio of sulfonate to backbone groups, which allows for direct calculation of λ from V_{water} in Eq. (5). Eqs. (2), (4), and (5) are used to calculate the conductivity for all layers other than the two adjacent to the SiO_2, using the fitted layer SLDs in Eq. (2). Eq. (4) is also used to calculate σ_{io} as a function of λ for the two layers adjacent to the SiO_2, but different approaches are used to calculate λ in these layers, depending on sample thickness. For t_{Naf} < 60 nm, phase segregation between the lamellae closest to the SiO_2 implies that the local EW ≠ 1100 g/mol, as indicated by V_{water} < 0 for the second layer of these samples (Fig. 3(b) below), which invalidates Eq. (5). For these samples, λ for the two layers adjacent to the SiO_2 are derived directly from the moles of H_2O and SO_3H in the 'atomistic profile' in our previous publication [64]. This profile is derived from simultaneous fits to t5 NR, humidified separately by H_2O and D_2O. For the two layers closest to the SiO_2 for t_{Naf} ≥ 60 nm, large interface widths cause the SLDs of the profiles shown in Fig. 3(c) to deviate from the fitted layer SLDs in the slab model. Therefore rather than using those fit parameters, the layer SLD used in Eq. (2) is the average minimum (first layer) or average maximum (second layer) layer SLD from the Fig. 3(c) profiles, averaged over all samples where t_{Naf} ≥ 60 nm. The resulting V_{water} values are then used in Eq. (5) to calculate λ values, for use in Eq. (4).

Again, these assumptions are intended as a first-order approximation. They are most likely accurate for the bulk-like layers in samples with t_{Naf} ≥ 60 nm, where the ionic domain morphology is similar to that for bulk Nafion. For thinner layers, and regions with lambda well

outside the normal range, factors other than λ undoubtedly influence the value of σ_{io}, including ionic domain size and morphology (concentration of SO_3H groups in each layer, lamellae vs. other ionic cluster shapes, *etc.*), and the tortuosity of the ionic domain interconnections. More accurate functional relationships can and should be developed, in future studies, for enhanced predictive capabilities.

In the present work, we use the approximations in Eqs. (4) and (5) as a starting estimate, and use scaling factors to fit these to published data [56]. The conductivity of a stack of layers with varying V_{water} is non-isotropic. We therefore calculate effective conductivities in the surface normal (σ_{normal}) and surface parallel () directions, as illustrated in Fig. 1(b). In the surface normal direction, transport is in series across the *j* layers in a film, and:

$$\sigma_{normal} = \frac{t_f}{\sum_j \frac{t_j}{\sigma_j}} \quad (6)$$

while the individual layers contribute in parallel in the surface-parallel direction:

$$\sigma_{parallel} = \frac{\sum_j \sigma_j t_j}{t_f}, \quad (7)$$

summed over all *j* layers in the film, where $t_f = \sum t_j$ is the total thickness of film *f*, and where the individual layer conductivities σ_j are calculated according to Eqs. (4) and (5) and scaled according to various models to fit experimental data, as described below. Pending better estimates, each layer's conductivity is assumed to be isotropic. Eqs. (6) and (7) establish a range of possible conductivity variations with varying thickness and interfacial structure.

3. Results and discussion

3.1. Neutron reflectometry data and fits

Fig. 2 shows the NR data (symbols) collected in H_2O-humidified vapor, along with the best fits (black lines) for each sample. Three trends are notable in the Fig. 2 data. (*i*) As thickness increases, the period of the reflectivity oscillations (i.e. "Keissig fringes") associated with the total film thickness decreases, due to the inverse relationship between thickness and the fringe period ΔQ_z. (*ii*) Beginning with t7, a broad peak centered at $Q_z = 2.0\ nm^{-1}$ forms. This peak, associated with the Nafion-SiO_2 interfacial lamellae, is more easily distinguished once the lamellar and total film thicknesses are appreciably different. (*iii*) For $t_{Naf} \geq 60$ nm, the lamellar peak height increases and the center shifts to $Q_z \sim 1.8\ nm^{-1}$, implying that the lamellae are thicker and more water rich.

Fig. 3 provides a summary of the fitted SLD profiles, including the best fits (solid lines) and 68% confidence intervals (shaded regions) for the entire sample (Fig. 3a) and for the lamellar region for $t_{Naf} < 60$ nm (Fig. 3b), and $t_{Naf} \geq 60$ nm (Fig. 3c). Fig. 3a shows that the bulk-like layer SLD decreases with increasing thickness, up to $t_{Naf} = 60$ nm, consistent with the increasing water uptake observed previously [61]. In Fig. 3b, the first water-poor layer (centered at roughly $z = 1.7$ nm) has an SLD higher than that of dry Nafion, consistent with the phase segregation of the Nafion polymer moieties between the layers for ultrathin Nafion [63]. For $t_{Naf} \geq 60$ nm, (Fig. 3c), these layers have SLDs less than or equal to that of dry Nafion, and in general have lower SLDs and thicker water-rich lamellae than the profiles in Fig. 3b, providing evidence of greater water uptake in the lamellae for $t_{Naf} \geq 60$ nm. While $SLD \leq SLD_{Nafion}$ for all layers in Fig. 3(c), phase segregation of the Nafion moieties is still likely, with the lower SLD due to greater water uptake than for the thinner samples in Fig. 3(b).

Table S2 in the Supporting information summarizes the NR fitting results, including reduced χ^2, t_{Naf}, and water volume fractions (V_{water}) for the interfacial lamellae region, bulk-like layer, and overall sample average. Throughout the paper, numbers in brackets represent 68% confidence intervals, the calculation of which is described elsewhere [81,84]. Note that the $V_{water,lamellae}$ values assume that each layer consists of only water and Nafion 1100, as described by Eq. (2). This approximation (necessary due to having data for only one water isotope) neglects the segregation of fluorocarbon and SO_3H groups, but has minimal impact on the value of $V_{water,lamellae}$ (on the order of 1–3%, when averaged over all lamellae).

Finally, for samples t103 and t120, suitable fits were obtained only after an additional layer was added at the free surface of the SLD profile, with equal likelihood of an SLD consistent with a fluorocarbon-rich (shown) or water-rich composition. As described in the Supporting information, the fluorocarbon-rich skin is considered the more likely model, due to its consistency with previous reports in the literature [23,85–88].

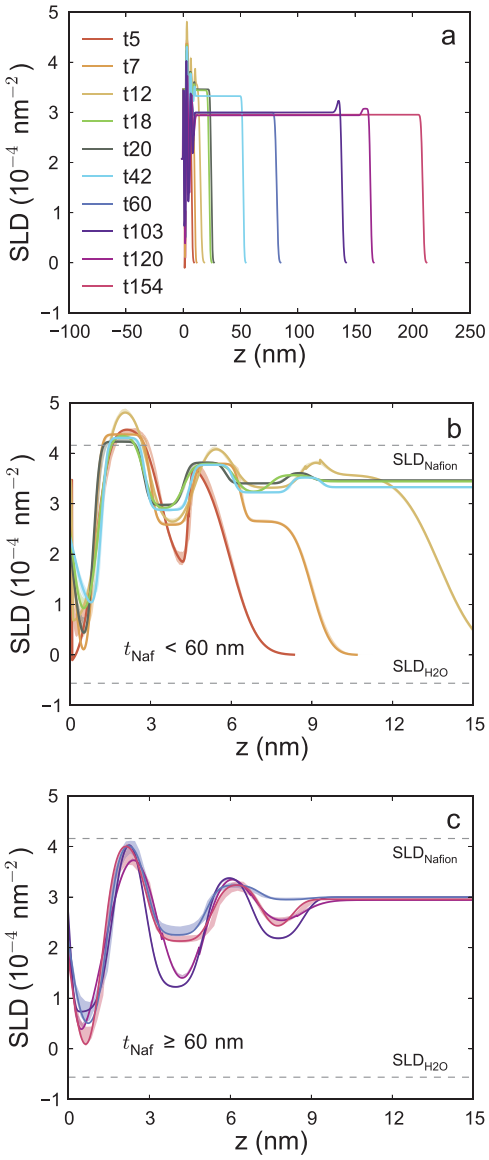

Fig. 3. Nafion SLD profiles, including best fits (solid lines) and 68% confidence intervals (shaded regions). SLDs are interpreted as a weighted average of H_2O ($-0.56*10^{-4}\ nm^{-2}$) and Nafion 1100 ($4.17*10^{-4}\ nm^{-2}$), shown by the dashed lines in Figs. (b) and (c). (a) Full profiles, including lamellae (z < 12 nm) and outer layer (z ≥ 12 nm). Outer layer water uptake increases with thickness for $t_{Naf} < 60$ nm, and is constant for $t_{Naf} \geq 60$ nm; (b) Focus on lamellar regions for *t*Naf < 60 nm; (c) Focus on lamellar region for *t*Naf ≥ 60 nm. Results show higher water content in the lamellae for $t_{Naf} \geq 60$ nm.

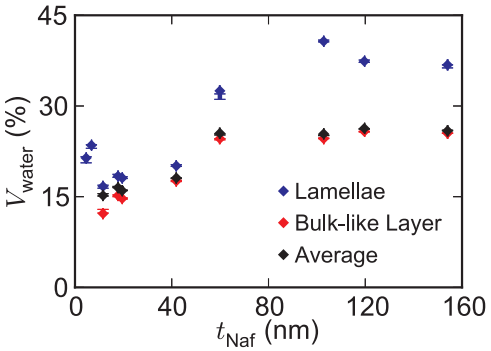

Fig. 4. Water volume fraction as a function of equivalent Nafion thickness t_{Naf}, including the interfacial lamellae, bulk-like layer, and whole-film average. Results show increasing influence of the water-rich lamellae as the total film thickness decreases. Error bars represent 68% confidence intervals in the fits and do not include systematic error or sample-to-sample variations.

3.2. Water content of ultrathin Nafion films

Fig. 4 shows the water volume fraction as a function of film thickness, averaged over three different regions of the sample: (*i*) $V_{water,lamellae}$: the lamellar region, (*ii*) $V_{water,bulk\text{-}like}$: the bulk-like layer plus surface layer (when present), and (*iii*) $V_{water,average}$: the entire sample (i.e. regions *i* and *ii*). For samples with $t_{Naf} \leq 7$ nm, no bulk-like layer is present, and hence $V_{water,laemllae}$ (shown) equals $V_{water,average}$. The Nafion water uptake falls into three distinct regimes:

3.2.1. Truncated regime

For t5 and t7, the film consists entirely of lamellae, since the film is 'truncated' before it reaches a thickness where the bulk-like layer forms. The lamellae are on average more water-rich than for the subsequent "thin-film" regime, mainly due to a high water volume fraction in the water rich layers.

3.2.2. Thin-film regime

For 7 nm $< t_{Naf} <$ 60 nm, a thin bulk-like layer (which increases its water uptake with increasing thickness) is present between the lamellae and the vapor environment. The lamellar region contains 6 layers with a relatively constant thickness. The lamellar water uptake is lower than for the truncated regime, but also increases with thickness, remaining slightly higher than $V_{water,bulk\text{-}like}$.

3.2.3. Thick-film regime

For $t_{Naf} \geq$ 60 nm, both $V_{water,lamellae}$ and $V_{water,bulk\text{-}like}$ increase significantly, relative to the values in the other two regimes. While $V_{water,bulk\text{-}like}$ is relatively constant in this regime, $V_{water,lamellae}$ has significant scatter. It is unclear whether this scatter is real or whether it represents systematic uncertainty and/or sample-to-sample variability in fabrication and thermal history. As such, we refrain from physical interpretation of these variations, herein.

Comparing V_{water} in different regions of the sample in Fig. 4 demonstrates the importance of depth profiles to explain the variations in water uptake with Nafion film thickness. The total water uptake, $V_{water,average}$, shows trends similar to previous studies which measured the water uptake of the sample as a whole. In those studies, V_{water} was constant above roughly 60 nm thickness, decreased with decreasing thickness between 20 nm and 60 nm, and then increased for films thinner than roughly 20 nm. While these trends may appear difficult to explain in terms of the *average* water uptake, considering the lamellae and bulk-like layer separately provides an explanation. As the sample thickness decreases below $t_{Naf} =$ 60 nm, the lamellae remain water rich (relative to the bulk-like layer). They also have a constant thickness, and therefore make up a greater fraction of the total sample, which tends to increase the average sample water content. For thicker bulk-like layers, the decrease in $V_{water,bulk\text{-}like}$ with decreasing thickness dominates over this effect. However, below roughly $t_{Naf} =$ 20 nm, the two effects roughly cancel ($V_{water,average}$ is roughly constant with thickness below 20 nm, in Fig. 4). As thickness decreases further, into the truncated regime, $V_{water,average}$ increases, relative to the 'thin-film' regime. While not definitive, the increasing importance of the water-rich lamellae with decreasing film thickness offers one plausible explanation for the previously observed increase in water uptake with decreasing thickness for very thin Nafion [57,59].

The transition between the thin- and thick-film regimes coincides with the point where the bulk-like layer thickness exceeds Nafion's radius of gyration, R_g. Measurements show $R_g =$ 40–50 nm in PEMFC catalyst inks [89], while $t_{bulk\text{-}like} =$ 41.8 nm for sample t42 and 72.1 nm for sample t60. The reduced dimensional confinement in the thick-film regime bulk-like layer correlates with increased mobility and plasticity, enabling greater water uptake ($\lambda = 10$), equal to that observed in bulk Nafion 1100 membranes. This is consistent with previous results from Eastman et al., who found a "frustrated packing" of the ionic domains for $t_{Naf} <$ 60 nm, where the domains are spaced further apart, less well-ordered, and contain less water than for $t_{Naf} \geq$ 60 nm [62].

The results demonstrate that the lamellar water uptake is influenced by interactions with both the substrate and the bulk-like layer (or with the vapor interface, in the truncated regime). In the truncated regime, $V_{water,lamellae}$ ranges from 21% to 24%. In the thin-film regime, when the bulk-like layer forms, $V_{water,lamellae}$ immediately drops to 16.7% [16.4, 16.9]%, and then both $V_{water,lamellae}$ and $V_{water,bulk\text{-}like}$ increase with increasing bulk-like layer thickness, up to R_g. In the thick-film regime, $V_{water,bulk\text{-}like}$ increases to a relatively constant 25.1 ± 0.7%, but $V_{water,lamellae}$ increases by an even greater amount, and ranges from 31.1% to 40.9%. The large non-monotonic and discontinuous shifts in lamellar water uptake in the different regimes—despite a constant substrate, temperature, and vapor RH—demonstrate the influence of the bulk-like layer morphology and water uptake on the lamellae.

To better understand the relationship between the water uptake in the lamellar and bulk-like regions, the moving "local average" water content, $V_{water,avg}$, is plotted as a function of distance from the substrate in Fig. 5, for the thin-film and thick-film regimes. Because the Nafion moieties phase-segregate between the layers in the lamellae [64], the Nafion stoichiometry (1100 EW) is only preserved when averaging over multiple neighboring layers. $V_{water,avg}$ in Fig. 5 is calculated from the NR fits as the water content of a given layer, plus half of each of its nearest neighbors (with each contribution weighted by its thickness). Calculation details are given in the Supporting information.

As seen in Fig. 5(a), the local average water uptake in the thin-film regime equals that of the bulk-like layer for all but the 2 layers closest to the SiO_2 interface, thereby giving rise to the slight overall increase of the lamellar water uptake compared to the bulk-like layer in Fig. 4. In the thick-film regime, the local water volume fraction decreases roughly continuously from ~40% at the SiO_2 interface to ~24% at the bulk-like layer. This may indicate either greater coupling between the lamellae and bulk-like layer in the thin-film regime, or that the rate of decline in $V_{water,avg}$ near the SiO_2 substrate is similar for both the thin- and the thick-film regime (which starts with a higher water content).

3.3. Ionic conductivity of thin-film nafion

These results emphasize the importance of in situ depth profiles in revealing not just *how much* water is retained in the film, but *how it is distributed*. While the exact transport mechanisms in thin-film CL Nafion remain poorly understood, it is well documented that ion conductivity in bulk Nafion is a non-linear function of the water content (due to the non-linear dependence of λ on V_{water}, described by Eq. (5)). If a similar dependence holds for thin-film Nafion, transport rates in the lamellae cannot be accurately estimated from the average water content of the film. For example, in the in-plane direction, where layer resistivities add in parallel, varying water uptake in the layers would produce a

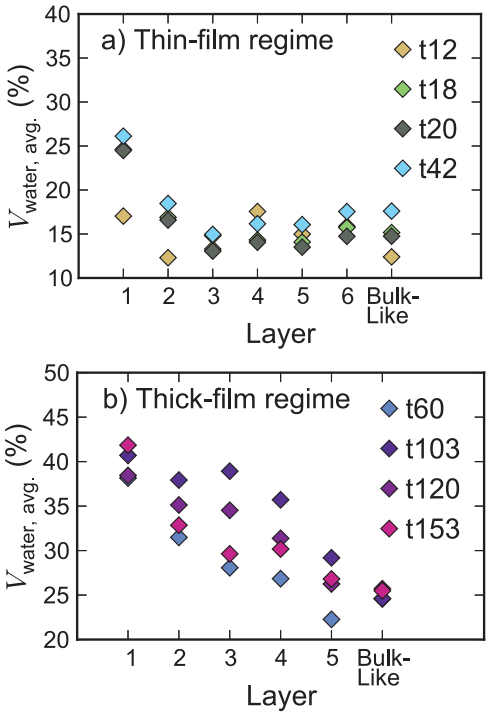

Fig. 5. "Local average" water content in lamellae, as a function of layer number. This approach accounts for phase-segregation of Nafion moieties between the lamellae, as described in Eqs. (S1)–(S3). (a) Thin-film regime. (b) Thick-film regime. Results reveal a shift in the water uptake profile between the thin-film and thick-film regimes, with V_{water} varying more continuously between the substrate and bulk-like layer in the thick-film regime.

different total conductivity than that estimated assuming a single layer with average water uptake. However, in the interfacial lamellae, the tortuosity and likely the internal structure of the ionic domains differ from bulk-like material, giving rise to a different dependence of conductivity on λ than represented in Eq. (4). Even in layers where the ionic domain morphology is similar to bulk samples, dimensional confinement effects can depress the conductivity by restricting the mobility of the polymer chains.

To estimate structure-property relationships in thin-film Nafion, we use the NR results above to predict in-plane ionic conductivities and compare these to experimental results for similar thicknesses, measured and published by Karan and colleagues (Paul et al. [56]). Relationships for bulk-like Nafion are used as a starting estimate for the thin-film conductivity, following Eqs. (4)–(7), as described in Section 2.3. These predictions (Supporting information Fig. S2) are greater at all thicknesses than the measured values from Paul et al. [56] The Fig. S2 predictions reflect the influence of reduced water uptake, but additional phenomena result in further deviations from the bulk conductivity. To estimate the dependence of the conductivity on the polymer microstructure, we propose four separate models for modifying the layer conductivities in Eq. (4):

- Model 1 (1 parameter): The ionic conductivities for all layers in the sample are multiplied by a single scaling factor f_{film}.
- Model 2 (2 parameters): The conductivity of the bulk-like layer (and surface layer, if applicable) is multiplied by $f_{bulk\text{-}like}$, and the conductivities of the lamellae are multiplied by $f_{lamellae}$.
- Model 3 (2 parameters): The conductivity of the bulk-like layer (and surface layer, if present) is multiplied by $f_{bulk\text{-}like}$. Conductivity values for all other layers are multiplied by a linear gradient of scaling factors from $f_{interface}$ to $f_{bulk\text{-}like}$, such that the scaling factor of the i^{th} lamellae is:

$$f_{lamellae,i} = \frac{N_{lamellae}-i}{N_{lamellae}} f_{interface} + \frac{i-1}{N_{lamellae}} f_{bulk-like}, \quad (8)$$

where $N_{lamellae}$ is the total number of lamellae in the sample and i is the lamella number ($i = 1$ indicates the layer adjacent to the SiO_2 substrate).

- Model 4 (3 parameters): The conductivity of the bulk-like layer (and surface layer, if applicable) is multiplied by $f_{bulk\text{-}like}$. The conductivity for each lamella i is multiplied by a linear gradient of scaling factors from $f_{lamellae,A}$ to $f_{lamellae,B}$, such that the scaling factor of the i^{th} lamella is:

$$f_{lamellae,i} = \frac{N_{lamellae}-i}{N_{lamellae}-1} f_{lamellae,A} + \frac{i-1}{N_{lamellae}-1} f_{lamellae,B}, \quad (9)$$

where $N_{lamellae}$ is the total number of lamellae in the sample and i is the lamella number ($i = 1$ indicates the layer adjacent to the SiO_2 substrate).

The scaling factor gradients for Models 3 and 4 hypothesize that the relationship between λ and σ varies with the distance from the SiO_2 substrate, which is supported by previous classical MD simulations [75]. Closer to the SiO_2, water uptake departs significantly from that in the bulk-like layer, Nafion moieties phase segregate between layers, and layers are likely stiffer due to bonding to the SiO_2 substrate. Other models, which propose that the scaling factor adjacent to the SiO_2 substrate is different from that in all other layers, were considered but fit the data poorly. They are reported in the Supporting information.

The scaling factors f_{film}, $f_{bulk\text{-}like}$, $f_{lamellae}$, $f_{interface}$, $f_{lamella,A}$, and $f_{lamellae,B}$ were fit to minimize the sum of squared residuals (SSR) between predicted and measured conductivities for each model; best fits are plotted in Fig. 6. Model 4 provides the best fit (SSR = 0.001), with $f_{lamellae,A} = 0.225$, $f_{lamellae,B} = 0.503$, and $f_{bulk\text{-}like} = 0.672$. The fits imply that the scaling factor in the bulk-like layer is greater than that in the lamellae, and in the lamellae it varies as a function of proximity to the SiO_2 substrate (lower scaling factors, or greater deviation from Eq. (4), closer to the substrate).

The results in Fig. 6 therefore provide insight into thin-film Nafion transport limitations, via reasonable conductivity values for sample layers. But the relevance for PEMFC performance is limited, because (*i*) the average conductivity at $T = 30$ °C is not very sensitive to film thickness < 100 nm, and (*ii*) PEMFCs are typically run at $T > 30$ °C. While Model 4 clearly fits better than Model 2, for example, it is not clear whether this leads to significantly better predictive capabilities at relevant temperatures.

To explore the variation of thin-film Nafion conductivity as a

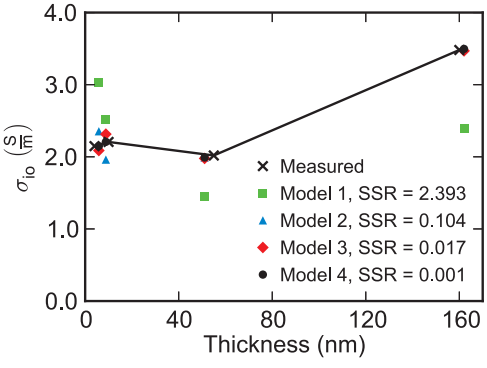

Fig. 6. Measured (×) and predicted (filled symbols) lateral conductivities for Nafion thin-films at 30 °C with varying thickness. Predicted σ_{io} values come from NR composition profiles, using Eqs. (2), (4), (5), and (7), which are scaled according to one of four models for how confinement and the lamellar morphology affect ionic conductivity. SSR for each model represents the sum of squared residuals. Experimental data from Paul et al. [56] Lines are drawn to connect experimental data points for ease of visualization.

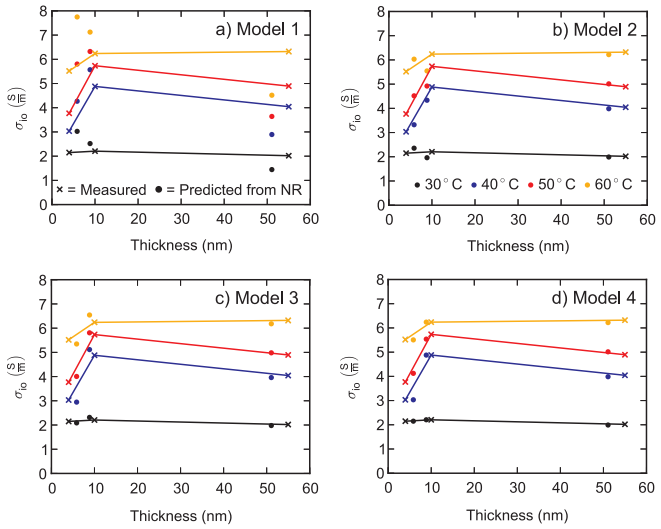

Fig. 7. In-plane ionic conductivity as a function of temperature and film thickness, for the four conductivity models fitted to the experimental data in Fig. 6. × = Experimental data from Paul et al. [56] with lines drawn to connect the data points for ease of visualization. • = Prediction from NR. Results show that the insights from models 3 and 4, in which the ion mobility varies throughout the film thickness (both bulk-like layer vs. lamellae, and within the lamellae) are required to predict and explain conductivity trends with varying thickness at relevant operating temperatures.

function of thickness at elevated temperatures, activation energies were fit to the data from Paul et al. [56] (described in detail in the Supporting information), and used to extend the conductivity predictions for all four models to T = 40, 50, and 60 °C. The results are shown in Fig. 7, focusing on thicknesses below 100 nm. Results for Models 1 and 2 show significant discrepancies between the predicted and measured data at elevated temperatures, whereas Models 3 and 4 show excellent agreement with the measured data. Model 3 provides suitable qualitative fits at all temperatures and thicknesses, while Model 4 gives the best quantitative fit. Statistical analysis could determine whether the extra fitting parameter in Model 4 is justified by the lower SSR. However, attempting to discriminate between Models 3 and 4 obscures the larger conclusion: regardless of whether Model 3 or Model 4 is statistically better, the model fitting demonstrates that the ion conductivity is significantly limited in all layers (relative to that for bulk samples with similar water content), and that the discrepancy is strongest at the substrate interface. Moreover, Fig. 7 demonstrates that the scaling factors in Eqs. (8) and (9) lead to accurate conductivity predictions at elevated temperatures.

Fig. 8 shows the individual layer conductivities and sample average conductivities $\sigma_{parallel}$ and σ_{normal} for Model 4 (Fig. 7d), extrapolated to T = 50 °C for samples t5, t7, and t42. The layer conductivities help explain the measured conductivity trends with increasing thickness, and show the importance of the composition depth profile when predicting conductivity in the CL. For samples t5 and t7, both in the 'truncated' regime, we see very high conductivities in the water-rich lamellae, and very low conductivities in the water-poor lamellae. The major difference between samples t5 and t7 is that sample t7 has one additional water-rich layer, at the Nafion-vapor interface, whereas t5 terminates with a thin, very low conductivity (σ_{io} = 0.46 S/m) layer. Hence, increasing the total thickness by just 2.2 nm is associated with large conductivity increases: $\sigma_{parallel}$ increases by 1.46 S/m (35%) and σ_{normal} by 1.64 S/m (135%). In the 'thin-film' regime (sample t42), the water-rich layer adjacent to the SiO_2 retains a high conductivity, but the conductivities of the subsequent water-rich layers quickly decay toward that of the bulk-like layer, as their water content decreases. The water-poor lamellae conductivities for t42 are generally equal to those found in the 'truncated' regime. However, for t42 we observe that the sample average conductivities $\sigma_{parallel}$ and σ_{normal} are roughly equal to

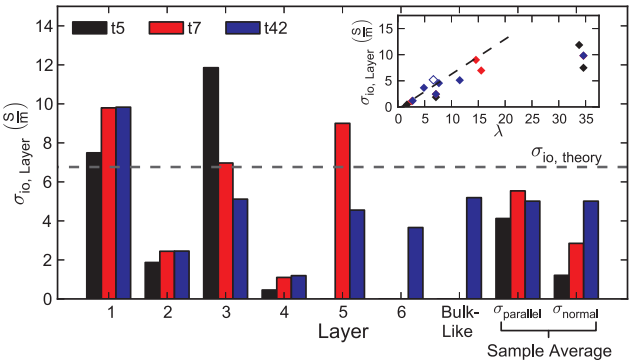

Fig. 8. Layer conductivities for samples t5, t7, and t42, plus sample average conductivities $\sigma_{parallel}$ and σ_{normal}, at T = 50 °C, calculated using Model 4, as described in the text. Results explain the non-monotonic conductivity trends with increasing thickness and the significant anisotropy in sample t5. $\sigma_{io,theory}$ is the conductivity for bulk Nafion membranes at RH = 92% and T = 50 °C. Inset shows layer conductivity vs. λ, the moles of water per mole of SO_3H for each layer. Results follow trends for bulk Nafion 1100 [43] (dashed line) for low λ, are depressed slightly for moderate λ, and show limiting behavior for λ greater than roughly 16. Open symbol is for the bulk-like layer in sample t42.

($\sigma_{parallel}$) or greater than (σ_{normal}) those found in the truncated regime, largely owing to the dominating influence of the thick bulk-like layer on the average conductivity values.

The Fig. 8 inset plots the layer conductivities for each sample as a function of λ (symbols), along with the predicted conductivity for bulk Nafion 1100 in the range $0 \le \lambda \le 22$ (dashed line), as established by Eq. (4) [43]. The conductivity in the lamellae generally follows bulk sample trends vs. λ, over the range for which Eq. (4) is valid, $\lambda < 16$. The conductivities closely match Eq. (4) at low water uptake ($\lambda \le 5$), are slightly depressed at moderate water uptake ($5 < \lambda \le 16$), and show limiting behavior for very high water uptake ($\lambda > 16$). Regardless of their water uptake, the lamellae do not exceed the conductivity for Nafion equilibrated with liquid water (λ = 22). These results explain the scaling factors used to fit the sample average conductivities in Figs. 6 and 7 – reduced scaling factors near the substrate do not imply reduced mobility, but rather demonstrate that the empirical relationship between λ and σ (Eq. (4)) cannot be extrapolated beyond the λ range for which it has been validated ($\lambda \le 22$). Moreover, segregation into water-rich and water-poor Nafion layers suppresses the sample average conductivity, relative to that calculated using the average water content.

We see, however, that for the bulk-like layer in the thin-film regime (i.e. sample t42, open symbol), the conductivity is roughly equal to the predicted value, based solely on its water content λ. While the bulk-like layer conductivity remains lower than that for bulk membranes at T = 50 °C and RH = 92%, it is consistent with the reduced water uptake in this layer, relative to bulk membranes, and therefore additional factors such as confinement are not required to explain the discrepancy in the conductivity values.

The presence of lamellae in CL Nafion may therefore impact PEMFC performance, due to varying transport limitations with varying agglomerate dimensions. The Nafion thicknesses explored above may represent the distance between carbon support particles within the agglomerate, or may represent the thickness of a Nafion 'shell' coating the agglomerate. While SiO_2 is not a technologically relevant substrate for the PEMFC CL, previous work shows that a smaller number of lamellae form on bare Pt substrates, and so the detailed characterization here provides quantitative insight into the effects of similar structures on Pt [73–75]. Furthermore, other factors such as Pt oxidation in the cathode or intentionally engineered surface functionalization of carbon support particles may lead to formation of lamellar regions more similar to those shown above. Finally, these results on a hydrophilic surface may have direct bearing on the enhanced conductivity observed in the presence of hydrophilic nanoparticle fillers [90–93].

It is therefore worth considering, in the context of Fig. 8, the 'ideal' Nafion thickness for PEMFC CL agglomerates. First, it bears repeating that transport within the agglomerates is a complex, three-dimensional process, and that transport will occur both parallel and normal to the substrate interface, as illustrated in Fig. 1. The ideal ionomer, therefore, has high and largely isotropic conductivities (i.e. high values for both $\sigma_{parallel}$ and σ_{normal}). Nafion thickness is also important: transport losses in the surface normal direction scale with the quotient t_{film}/σ_{normal}. Of the three samples in Fig. 8, t42 has the highest σ_{normal} value, but the quotient $t_{film}/\sigma_{normal} = 1.02 \times 10^{-8}$ W-m^2, whereas it is 3.6×10^{-9} W-m^2 for sample t5 and 2.1×10^{-9} W-m^2 for sample t7. Losses in the surface parallel direction, meanwhile, scale with $1/(t_{film} \times \sigma_{parallel})$. This quotient is 5.61×10^7 W for t5, 3.09×10^7 W for t7, and 3.9×10^6 W for t42. While, it is not realistic to expect control of the ionomer thickness with sufficient precision or uniformity to differentiate between thicknesses corresponding to samples t5 and t7, for example, one might expect control on the level of the regimes. The results suggest that ionomer films in the 'truncated' regime will minimize transport losses normal to the lamellae, relative to those in the 'thin-film' regime (losses are a factor of 3 lower in t7 than in t42), but that ionomers in the 'thin-film' regime will minimize losses parallel to the lamellae (losses are a factor of 5 lower in t42 than in t7). Extending these predictions to continuum-level PEMFC CL simulations to directly determine implications for PEMFCs is the topic of a forthcoming publication from our group. Truly predictive simulations to guide PEMFC design will require enhanced characterization of the CL agglomerate microstructure and the morphology of the ionomer phase located therein.

These results also motivate better understanding of the ion transport properties of thin-film Nafion as a function of the ionomer morphology and local water uptake (e.g., to replace Eqs. (4) and (5)). The measurements and simulations herein provide one promising avenue to reveal such structure-property relationships. Because NR is capable of measuring length scales from 1.5 nm up to several 100 nm, all with sub-Ångström spatial resolution, NR results are directly relevant to both computational chemistry approaches (such as those demonstrated by Damasceno Borges et al. [75]) and continuum-scale experiments and simulations.

4. Conclusions

For ionic copolymers in a range of established and emerging technologies, phase segregation at material interfaces influences structure-property relationships and device performance. This study demonstrates the importance of spatial morphology variations in thin-films or coatings when determining average properties, and presents a means to deconvolute the effects of thickness, substrate, and chemical environment on thin-film copolymer properties. Via in situ NR of ultra-thin Nafion films with an equivalent thickness ranging from 5 to 153 nm, we observe three separate thickness regimes. In the truncated regime, the entire sample consists of lamellae. For thicker films, a non-lamellar bulk-like layer is added. The samples with a bulk-like layer were further differentiated into the thin-film regime with equivalent thickness $\leq$ 42 nm and hydrated thickness $\leq$ 51 nm and a thick-film regime with equivalent thickness $\geq$ 60 nm and hydrated thickness $\geq$ 81 nm. The transition between regimes roughly coincides with the point where the bulk-like layer thickness exceeds the radius of gyration for thin-film Nafion. The bulk-like layer of the thick-film regime absorbs the same amount of water as in bulk membranes ($\lambda = 10$), whereas in the thin-film regime the water uptake of the bulk-like layer decreases with decreasing thickness. Results also demonstrate that water uptake in the lamellae is influenced by interactions with both the SiO_2 substrate and either the vapor interface or the bulk-like layer. Finally, detailed water uptake depth profiles provide an explanation for the previously observed increase in water uptake for films thinner than 20 nm.

The depth profiles from NR fitting are used to model the thin-film ionic conductivity parallel to and normal to the substrate plane. Fitting to previously published experimental results demonstrates that, at length scales relevant to PEMFC CL agglomerates, lamellae can contribute to anisotropic transport limitations, such that small changes in ionomer thickness can lead to significant variations in the average ion conductivity. Additional work is required to establish the prevalence of the lamellar structures in PEMFC CL agglomerates and to precisely determine their impact on ion transport therein.

Acknowledgements

The authors are grateful for the support of the National Academies' NRC Research Associateship Program (SD), as well as additional support provided by the Center for High Resolution Neutron Scattering, a partnership between the National Institute of Standards and Technology and the National Science Foundation under Agreement No. DMR-1508249, through the NIST Summer Undergraduate Research Fellowship program (AM, PB). SD thanks and the Center for High Performance Computing at Colorado School of Mines for providing a platform to run Refl1D simulations.

Supporting information available

Supporting Information is available, and includes additional details regarding: (*i*) Nafion thin-film fabrication, (*ii*) NR fitting results, (*iii*) Surface layers in the thick-film regime, (*iv*) Calculation of average lamellar water content as a function of distance from the substrate, (*v*) Predicted conductivities using bulk Nafion relationships, (*vi*) Alternative conductivity scaling models, and (*vii*) Calculation of activation energies for thin-film Nafion conductivity.

Appendix A. Supplementary material

Supplementary data associated with this article can be found in the online version at http://dx.doi.org/10.1016/j.nanoen.2018.01.008.

References

[1] A. Kusoglu, A. Kwong, K.T. Clark, H.P. Gunterman, A.Z. Weber, Water uptake of fuel-cell catalyst layers, J. Electrochem. Soc. 159 (2012) F530–F535, http://dx.doi.org/10.1149/2.031209jes.
[2] B. Kientiz, H. Yamada, N. Nonoyama, A.Z. Weber, Interfacial water transport effects in proton-exchange membranes, J. Fuel Cell Sci. Technol. 8 (2011) 11013, http://dx.doi.org/10.1115/1.4002398.
[3] J.D. Fairweather, D. Spernjak, A.Z. Weber, D. Harvey, S. Wessel, D.S. Hussey, D.L. Jacobson, K. Artyushkova, R. Mukundan, R.L. Borup, Effects of cathode corrosion on through-plane water transport in proton exchange membrane fuel cells, J. Electrochem. Soc. 160 (2013) F980–F993, http://dx.doi.org/10.1149/2.024309jes.
[4] N. Nonoyama, S. Okazaki, A.Z. Weber, Y. Ikogi, T. Yoshida, Analysis of oxygen-transport diffusion resistance in proton-exchange-membrane fuel cells, J. Electrochem. Soc. 158 (2011) B416, http://dx.doi.org/10.1149/1.3546038.
[5] D.K. Paul, A. Fraser, K. Karan, Towards the understanding of proton conduction mechanism in PEMFC catalyst layer: conductivity of adsorbed Nafion films, Electrochem. Commun. 13 (2011) 774–777, http://dx.doi.org/10.1016/j.elecom.2011.04.022.
[6] D. Paul, A. Fraser, J. Pearce, K. Karan, Understanding the ionomer structure and the proton conduction mechanism in PEFC catalyst layer: adsorbed nafion on model substrate, ECS Trans. 41 (2011) 1393–1406, http://dx.doi.org/10.1149/1.3635670.
[7] M. Secanell, K. Karan, A. Suleman, N. Djilali, Multi-variable optimization of PEMFC cathodes using an agglomerate model, Electrochim. Acta 52 (2007) 6318–6337, http://dx.doi.org/10.1016/j.electacta.2007.04.028.
[8] A.Z. Weber, A. Kusoglu, Unexplained transport resistances for low-loaded fuel-cell catalyst layers, J. Mater. Chem. A. 2 (2014) 17207–17211, http://dx.doi.org/10.1039/C4TA02952F.
[9] R.M. Darling, A.Z. Weber, M.C. Tucker, M.L. Perry, The influence of electric field on crossover in redox-flow batteries, J. Electrochem. Soc. 163 (2015) A5014–A5022, http://dx.doi.org/10.1149/2.0031601jes.
[10] I. Bauer, S. Thieme, J. Brückner, H. Althues, S. Kaskel, Reduced polysulfide shuttle in lithium–sulfur batteries using Nafion-based separators, J. Power Sources 251 (2014) 417–422, http://dx.doi.org/10.1016/j.jpowsour.2013.11.090.
[11] N. Wang, S. Peng, D. Lu, S. Liu, Y. Liu, K. Huang, Nafion/TiO2 hybrid membrane fabricated via hydrothermal method for vanadium redox battery, J. Solid State Electrochem. 16 (2012) 1577–1584, http://dx.doi.org/10.1007/s10008-011-1560-z.

[12] X. Wu, J. Hu, J. Liu, Q. Zhou, W. Zhou, H. Li, Y. Wu, Ion exchange membranes for vanadium redox flow batteries, Pure Appl. Chem. 86 (2014), http://dx.doi.org/10.1515/pac-2014-0101.

[13] S. Kumari, R. Turner White, B. Kumar, J.M. Spurgeon, N.S. Lewis, D.G. Nocera, M. Gratzel, A.J. Bard, M.A. Fox, M.G. Walter, et al., Solar hydrogen production from seawater vapor electrolysis, Energy Environ. Sci. 9 (2016) 1725–1733, http://dx.doi.org/10.1039/C5EE03568F.

[14] P. Millet, R. Ngameni, S.A. Grigoriev, N. Mbemba, F. Brisset, A. Ranjbari, C. Etiévant, PEM water electrolyzers: from electrocatalysis to stack development, Int. J. Hydrog. Energy 35 (2010) 5043–5052, http://dx.doi.org/10.1016/j.ijhydene.2009.09.015.

[15] C. Rozain, P. Millet, Electrochemical characterization of polymer electrolyte membrane water electrolysis cells, Electrochim. Acta 131 (2014) 160–167, http://dx.doi.org/10.1016/j.electacta.2014.01.099.

[16] S. Siracusano, V. Baglio, N. Briguglio, G. Brunaccini, A. Di Blasi, A. Stassi, R. Ornelas, E. Trifoni, V. Antonucci, A.S. Aricò, An electrochemical study of a PEM stack for water electrolysis, Int. J. Hydrog. Energy 37 (2012) 1939–1946, http://dx.doi.org/10.1016/j.ijhydene.2011.06.019.

[17] S.M. Ayyadurai, A.D. Worrall, J.A. Bernstein, A.P. Angelopoulos, Perfluorosulfonic acid membrane catalysts for optical sensing of anhydrides in the gas phase, Anal. Chem. 82 (2010) 6265–6272, http://dx.doi.org/10.1021/ac101356j.

[18] K.-A. Frith, J.L. Limson, Reprint of "pH tuning of Nafion® for selective detection of tryptophan,", Electrochim. Acta 55 (2010) 4281–4286, http://dx.doi.org/10.1016/j.electacta.2010.03.098.

[19] Y. Lin, Q. zhou, Y. Lin, D. Tang, G. Chen, D. Tang, Simple and sensitive detection of aflatoxin B1 within five minute using a non-conventional competitive immunosensing mode, Biosens. Bioelectron. 74 (2015) 680–686, http://dx.doi.org/10.1016/j.bios.2015.07.029.

[20] M. Shariatgorji, J. Astorga-Wells, L.L. Ilag, Trends in the bioanalytical applications of microfluidic electrocapture, Anal. Bioanal. Chem. 399 (2011) 191–195, http://dx.doi.org/10.1007/s00216-010-4092-y.

[21] J. Zavazalova, M.E. Ghica, K. Schwarzova-Peckova, J. Barek, C.M.A. Brett, Carbon-based electrodes for sensitive electroanalytical determination of aminonaphthalenes, Electroanalysis 27 (2015) 1556–1564, http://dx.doi.org/10.1002/elan.201400719.

[22] A.B. Anderson, J. Roques, S. Mukerjee, V.S. Murthi, N.M. Markovic, V. Stamenkovic, Activation energies for oxygen reduction on platinum alloys: theory and experiment, J. Phys. Chem. B. 109 (2005) 1198–1203, http://dx.doi.org/10.1021/jp047468z.

[23] M. Bass, A. Berman, A. Singh, O. Konovalov, V. Freger, Surface structure of nafion in vapor and liquid, J. Phys. Chem. B 114 (2010) 3784–3790, http://dx.doi.org/10.1021/jp9113128.

[24] I. Bauer, M. Kohl, H. Althues, S. Kaskel, Shuttle suppression in room temperature sodium-sulfur batteries using ion selective polymer membranes, Chem. Commun. 50 (2014) 3208–3210, http://dx.doi.org/10.1039/c4cc00161c.

[25] I. Bauer, S. Thieme, J. Brueckner, H. Althues, S. Kaskel, Reduced polysulfide shuttle in lithium-sulfur batteries using Nafion-based separators, J. Power Sources 251 (2014) 417–422, http://dx.doi.org/10.1016/j.jpowsour.2013.11.090.

[26] L. Chen, L.L. Shaw, Recent advances in lithium–sulfur batteries, J. Power Sources 267 (2014) 770–783, http://dx.doi.org/10.1016/j.jpowsour.2014.05.111.

[27] E. Nasybulin, W. Xu, M.H. Engelhard, Z. Nie, X.S. Li, J.G. Zhang, Stability of polymer binders in Li-O_2 batteries, J. Power Sources 243 (2013) 899–907, http://dx.doi.org/10.1016/j.jpowsour.2013.06.097.

[28] C.V. Amanchukwu, J.R. Harding, Y. Shao-Horn, P.T. Hammond, Understanding the chemical stability of polymers for lithium–air batteries, Chem. Mater. 27 (2015) 550–561, http://dx.doi.org/10.1021/cm5040003.

[29] S. Ganapathy, B.D. Adams, G. Stenou, M.S. Anastasaki, K. Goubitz, X.-F. Miao, L.F. Nazar, M. Wagemaker, Nature of Li_2O_2 oxidation in a Li–O_2 battery revealed by operando X-ray diffraction, J. Am. Chem. Soc. 136 (2014) 16335–16344, http://dx.doi.org/10.1021/ja508794r.

[30] J.R. Harding, Y.-C. Lu, Y. Tsukada, Y. Shao-Horn, Evidence of catalyzed oxidation of Li2O2 for rechargeable Li–air battery applications, Phys. Chem. Chem. Phys. 14 (2012) 10540, http://dx.doi.org/10.1039/c2cp41761h.

[31] L. Qin, D. Zhai, W. Lv, W. Yang, J. Huang, S. Yao, J. Cui, W.-G. Chong, J.-Q. Huang, F. Kang, et al., A high-performance lithium ion oxygen battery consisting of Li_2O_2 cathode and lithiated aluminum anode with nafion membrane for reduced O_2 crossover, Nano Energy (2017), http://dx.doi.org/10.1016/j.nanoen.2017.08.029.

[32] F.I. Allen, L.R. Comolli, A. Kusoglu, M.A. Modestino, A.M. Minor, A.Z. Weber, Morphology of hydrated as-cast Nafion revealed through cryo electron tomography, ACS Macro Lett. 4 (2015) 1–5, http://dx.doi.org/10.1021/mz500606h.

[33] J.A. Elliott, D. Wu, S.J. Paddison, R.B. Moore, A unified morphological description of Nafion membranes from SAXS and mesoscale simulations, Softw. Matter 7 (2011) 6820, http://dx.doi.org/10.1039/c1sm00002k.

[34] G.S. Hwang, D.Y. Parkinson, A. Kusoglu, A. a Macdowell, A.Z. Weber, Understanding water uptake and transport in Nafion using X-ray microtomography, ACS Macro Lett. (2013) 2–5, http://dx.doi.org/10.1021/Mz300651a.

[35] X. Ren, T.D. Myles, K.N. Grew, W.K.S. Chiu, Carbon dioxide transport in Nafion 1100 EW membrane and in a direct methanol fuel cell, J. Electrochem. Soc. 162 (2015) F1221–F1230, http://dx.doi.org/10.1149/2.0711510jes.

[36] F. Xu, O. Diat, G. Gebel, A. Morin, Determination of transverse water concentration profile through MEA in a fuel cell using neutron scattering, J. Electrochem. Soc. 154 (2007) B1389, http://dx.doi.org/10.1149/1.2794287.

[37] M. Pineri, G. Gebel, R.J. Davies, O. Diat, Water sorption–desorption in Nafion® membranes at low temperature, probed by micro X-ray diffraction, J. Power Sources 172 (2007) 587–596, http://dx.doi.org/10.1016/j.jpowsour.2007.05.037.

[38] G. Gebel, O. Diat, S. Escribano, R. Mosdale, Water profile determination in a running PEMFC by small-angle neutron scattering, J. Power Sources 179 (2008) 132–139, http://dx.doi.org/10.1016/j.jpowsour.2007.12.124.

[39] G. Gebel, S. Lyonnard, H. Mendil-Jakani, A. Morin, The kinetics of water sorption in Nafion membranes: a small-angle neutron scattering study, J. Phys. Condens. Matter 23 (2011) 234107, http://dx.doi.org/10.1088/0953-8984/23/23/234107.

[40] S. Deabate, P. Huguet, A. Morin, G. Gebel, Y. Lanteri, Z. Peng, A.-K. Sutor, Raman microspectroscopy as a useful tool for in situ and operando studies of water transport in perfluorosulfonic membranes for PEMFCs, Fuel Cells 14 (2014) 677–693, http://dx.doi.org/10.1002/fuce.201300236.

[41] S. Deabate, G. Gebel, P. Huguet, A. Morin, G. Pourcelly, Y. Wang, K.S. Chen, J. Mishler, S.C. Cho, X.C. Adroher, et al., In situ and operando determination of the water content distribution in proton conducting membranes for fuel cells: a critical review, Energy Environ. Sci. 5 (2012) 8824, http://dx.doi.org/10.1039/c2ee21834h.

[42] M. Lopez-Haro, L. Guétaz, T. Printemps, A. Morin, S. Escribano, P.-H. Jouneau, P. Bayle-Guillemaud, F. Chandezon, G. Gebel, Three-dimensional analysis of Nafion layers in fuel cell electrodes, Nat. Commun. 5 (2014) 5229, http://dx.doi.org/10.1038/ncomms6229.

[43] T.E. Springer, T.A. Zawodzinski, S. Gottesfeld, Polymer electrolyte fuel cell model, J. Electrochem. Soc. 138 (1991) 2334, http://dx.doi.org/10.1149/1.2085971.

[44] T.A. Zawodzinski, T.E. Springer, F. Uribe, S. Gottesfeld, Characterization of polymer electrolytes for fuel cell applications, Solid State Ion. 60 (1993) 199–211, http://dx.doi.org/10.1016/0167-2738(93)90295-E.

[45] T.A. Zawodzinski, C. Derouin, S. Radzinkai, R.J. Sherman, V.T. Smith, T.E. Springer, S. Gottesfeld, Water uptake by and transport through nafion® 117 membranes, J. Electrochem. Soc. 140 (1993) 1041, http://dx.doi.org/10.1149/1.2056194.

[46] K. Schmidt-Rohr, Q. Chen, Parallel cylindrical water nanochannels in nafion fuel-cell membranes, Nat. Mater. 7 (2008) 75–83, http://dx.doi.org/10.1038/nmat2074.

[47] K.A. Mauritz, R.B. Moore, State of understanding of nafion, Chem. Rev. 104 (2004) 4535–4586, http://dx.doi.org/10.1021/cr0207123.

[48] W. Kubo, K. Yamauchi, K. Kumagai, M. Kumagai, K. Ojima, K. Yamada, Imaging of ionic channels in proton exchange membranes by the nickel replica method, J. Phys. Chem. C 114 (2010) 2370–2374, http://dx.doi.org/10.1021/jp9082695.

[49] L. Rubatat, G. Gebel, O. Diat, Fibrillar structure of nafion: matching fourier and real space studies of corresponding films and solutions, Macromolecules 37 (2004) 7772–7783, http://dx.doi.org/10.1021/ma049683j.

[50] L. Rubatat, A.L. Rollet, G. Gebel, O. Diat, Evidence of elongated polymeric aggregates in nafion, Macromolecules 35 (2002) 4050–4055, http://dx.doi.org/10.1021/ma011578b.

[51] K.-D. Kreuer, G. Portale, A critical revision of the nano-morphology of proton conducting ionomers and polyelectrolytes for fuel cell applications, Adv. Funct. Mater. 23 (2013) 5390–5397, http://dx.doi.org/10.1002/adfm.201300376.

[52] G. Gebel, Structural evolution of water swollen perfluorosulfonated ionomers from dry membrane to solution, Polymer 41 (2000) 5829–5838, http://dx.doi.org/10.1016/S0032-3861(99)00770-3.

[53] T.D. Gierke, G.E. Munn, F.C. Wilson, The morphology in nafion perfluorinated membrane products, as determined by wide- and small-angle x-ray studies, J. Polym. Sci. Polym. Phys. Ed. 19 (1981) 1687–1704, http://dx.doi.org/10.1002/pol.1981.180191103.

[54] S. Kim, K. No, S. Hong, Visualization of ion transport in Nafion using electrochemical strain microscopy, Chem. Comm. 52 (2016) 831–834.

[55] M.H. Litt, Reevaluation of Nafion morphology, Am. Chem. Soc. Polym. Prepr. 38 (1997) 80–81.

[56] D.K. Paul, R. Mccreery, K. Karan, Proton transport property in supported nafion nanothin films by electrochemical impedance spectroscopy, J. Electrochem. Soc. 161 (2014) 1395–1402, http://dx.doi.org/10.1149/2.0571414jes.

[57] A. Kusoglu, D. Kushner, D.K. Paul, K. Karan, M.A. Hickner, A.Z. Weber, Impact of substrate and processing on confinement of nafion thin films, Adv. Funct. Mater. 24 (2014) 4763–4774, http://dx.doi.org/10.1002/adfm.201304311.

[58] A.Z. Weber, R.L. Borup, R.M. Darling, P.K. Das, T.J. Dursch, W. Gu, D. Harvey, A. Kusoglu, S. Litster, M.M. Mench, et al., A critical review of modeling transport phenomena in polymer-electrolyte fuel cells, J. Electrochem. Soc. 161 (2014) F1254–F1299, http://dx.doi.org/10.1149/2.0751412jes.

[59] M.A. Modestino, D.K. Paul, S. Dishari, S.A. Petrina, F.I. Allen, M.A. Hickner, K. Karan, R.A. Segalman, A.Z. Weber, Self-assembly and transport limitations in Con fi ned Na fi on films, Macromolecules 46 (2013) 867–873, http://dx.doi.org/10.1021/ma301999a.

[60] C.-Y. Jung, S.-C. Yi, Influence of the water uptake in the catalyst layer for the proton exchange membrane fuel cells, Electrochem. Commun. 35 (2013) 34–37, http://dx.doi.org/10.1016/j.elecom.2013.07.037.

[61] K.A. Page, A. Kusoglu, C.M. Stafford, S. Kim, R.J. Kline, A.Z. Weber, Confinement-driven increase in ionomer thin-film modulus, Nano Lett. 14 (2014) 2299–2304, http://dx.doi.org/10.1021/nl501233g.

[62] S.A. Eastman, S. Kim, K.A. Page, B.W. Rowe, S. Kang, S.C. DeCaluwe, J.A. Dura, C.L. Soles, K.G. Yager, Correction to effect of confinement on structure, water solubility, and water transport in nafion thin films (571–571), Macromolecules 46 (2013), http://dx.doi.org/10.1021/ma302140d.

[63] J.A. Dura, V.S. Murthi, M. Hartman, S.K. Satija, C.F. Majkrzak, Multilamellar interface structures in nafion, Macromolecules 42 (2009) 4769–4774, http://dx.doi.org/10.1021/ma802823j.

[64] S.C. DeCaluwe, P.A. Kienzle, P. Bhargava, A.M. Baker, J.A. Dura, Phase segregation of sulfonate groups in Nafion interface lamellae, quantified via neutron reflectometry fitting techniques for multi-layered structures, Softw. Matter 10 (2014) 5763, http://dx.doi.org/10.1039/C4SM00850B.

[65] S. Kim, J.A. Dura, K.A. Page, B.W. Rowe, K.G. Yager, H.-J. Lee, C.L. Soles, Surface-induced nanostructure and water transport of thin proton-conducting polymer films, Macromolecules 46 (2013) 5630–5637, http://dx.doi.org/10.1021/ma400750f.
[66] E.M. Davis, C.M. Stafford, K.A. Page, Elucidating water transport mechanisms in nafion thin films, ACS Macro Lett. 2 (2014) 288–291.
[67] H.K. Shim, D.K. Paul, K. Karan, Resolving the contradiction between anomalously high water uptake and low conductivity of nanothin nafion films on SiO_2 substrate, Macromolecules 48 (2015) 8394–8397, http://dx.doi.org/10.1021/acs.macromol.5b02093.
[68] N.E. De Almeida, D.K. Paul, K. Karan, G.R. Goward, H solid-state NMR study of nanothin Na fi on films, J. Phys. Chem. C 119 (2015) 1280–1285, http://dx.doi.org/10.1021/jp5086747.
[69] D.K. Paul, K. Karan, Conductivity and wettability changes of ultrathin nafion films subjected to thermal annealing and liquid water exposure, J. Phys. Chem. C 118 (2014) 1828–1835, http://dx.doi.org/10.1021/jp410510x.
[70] J.A. Dura, E.D. Rus, P.A. Kienzle, B.B. Maranville, Nanolayer analysis by neutron reflectometry, in: T. Imae (Ed.), Nanolayer Research Methodology and Technology for Green Chemistry, Elsevier, Oxford, England, 2017.
[71] B. Hou, S. Kim, T. Kim, J. Kim, S. Hong, C.B. Bahn, C. Park, J.H. Kim, The hydration structure at yttria-stabilized cubic zirconia (110)-water interface with sub-Angstrom resolution, Sci. Rep. 6 (2016) 27916-1–27916-8.
[72] D.L. Wood, J. Chlistunoff, J. Majewski, R.L. Borup, Nafion structural phenomena at platinum and carbon interfaces, J. Am. Chem. Soc. 131 (2009) 18096–18104, http://dx.doi.org/10.1021/ja9033928.
[73] V.S. Murthi, J. Dura, S. Satija, C. Majkrzak, Water uptake and interfacial structural changes of thin film Nafion® membranes measured by neutron reflectivity for PEM fuel cells, ECS Trans. (2008) 1471–1485, http://dx.doi.org/10.1149/1.2981988.
[74] D.D. Borges, G. Gebel, A.A. Franco, K. Malek, S. Mossa, Morphology of supported polymer electrolyte ultrathin films: a numerical study, J. Phys. Chem. C 119 (2015) 1201–1216.
[75] D. Damasceno Borges, A.A. Franco, K. Malek, G. Gebel, S. Mossa, Inhomogeneous transport in model hydrated polymer electrolyte supported ultrathin films, ACS Nano 7 (2013) 6767–6773, http://dx.doi.org/10.1021/nn401624p.
[76] Y. Sone, Proton conductivity of Nafion 117 as measured by a four-electrode AC impedance method, J. Electrochem. Soc. 143 (1996) 1254, http://dx.doi.org/10.1149/1.1836625.
[77] M.A. Modestino, A. Kusoglu, A. Hexemer, A.Z. Weber, R.A. Segalman, Controlling Na fi on structure and properties via wetting interactions, Macromolecules 45 (2012) 4681–4688.
[78] S. Sharma, B.G. Pollet, Support materials for PEMFC and DMFC electrocatalysts - a review, J. Power Sources 208 (2012) 96–119.
[79] J. Liu, C.-T. Liu, L. Zhao, J.-J. Zhang, L.-M. Zhang, Z.-B. Wang, Effect of different structures of carbon supports for cathode catalyst on performance of direct methanol fuel cell, Int. J. Hydrogen Energy 41 (2016) 1859–1870.
[80] N. Karthikeyan, B.P. Vinayan, M. Rajesh, K. Balji, A.K. Subramani, S. Ramaprabhu, Highly durable platinum cbased cathdoe electrocatalysts for PEMFC application using oxygen and nitrogen functional groups attached nanocarbon supports, Fuel Cells 15 (2015) 278–287.
[81] P.A. Kienzle, J.A. Krycka, N. Patel, Refl1D: Interactive depth profile modeler (n.d. ⟨http://www.reflectometry.org/danse/software⟩.
[82] G. Schwarz, Estimating dimensions of a model, Ann. Stat. 6 (1978) 461–464.
[83] A.A. Shah, G.-S. Kim, P.C. Sui, D. Harvey, Transient non-isothermal model of a polymer electrolyte fuel cell, J. Power Sources 163 (2007) 793–806, http://dx.doi.org/10.1016/j.jpowsour.2006.09.022.
[84] J.E. Owejan, J.P. Owejan, S.C. DeCaluwe, J.A. Dura, Solid electrolyte interphase in Li-ion batteries: evolving structures measured in situ by neutron reflectometry, Chem. Mater. 24 (2012) 2133–2140, http://dx.doi.org/10.1021/cm3006887.
[85] R.P. Dowd, C.S. Day, T. Van Nguyen, Engineering the ionic polymer phase surface properties of a PEM fuel cell catalyst layer, J. Electrochem. Soc. 164 (2017) F138–F146, http://dx.doi.org/10.1149/2.1081702jes.
[86] K.B. Daly, J.B. Benziger, A.Z. Panagiotopoulos, P.G. Debenedetti, Molecular dynamics simulations of water permeation across nafion membrane interfaces, J. Phys. Chem. B 118 (2014) 8798–8807, http://dx.doi.org/10.1021/jp5024718.
[87] A. Kongkanand, Interfacial water transport measurements in nafion thin films using a quartz-crystal microbalance, J. Phys. Chem. C 115 (2011) 11318–11325, http://dx.doi.org/10.1021/jp2028214.
[88] P.W. Majsztrik, M.B. Satterfield, A.B. Bocarsly, J.B. Benziger, Water sorption, desorption and transport in Nafion membranes, J. Membr. Sci. 301 (2007) 93–106, http://dx.doi.org/10.1016/j.memsci.2007.06.022.
[89] T. Kusano, T. Hiroi, K. Amemiya, M. Ando, T. Takahashi, M. Shibayama, Structural evolution of a catalyst ink for fuel cells during the drying process investigated by CV-SANS, Polym. J. 47 (2015) 546–555, http://dx.doi.org/10.1038/pj.2015.36.
[90] I. Nicotera, V. Kosma, C. Simari, G.A. Ranieri, M. Sgambetterra, S. Panero, M.A. Navarra, An NMR study on the molecular dynamic and exchange effects in composite Nafion/sulfated titania membranes for PEMFCs, Int. J. Hydrog. Energy 40 (2015) 14651–14660, http://dx.doi.org/10.1016/j.ijhydene.2015.06.137.
[91] K.M. Lee, M.H. Jang, C.S. Han, S.T. Lee, J.H. Lee, S.K. Lim, Proton conducting composite membranes from Nafion and NH4 + /H3O + -beta -alumina for high temperature PEMFC, J. Ceram. Process. Res. 13 (2012) 461–465.
[92] S.Y. Jang, S.H. Han, Sulfonated polySEPS/hydrophilic-SiO_2 composite membranes for polymer electrolyte membranes (PEMs), J. Ind. Eng. Chem. 23 (2015) 285–289, http://dx.doi.org/10.1016/j.jiec.2014.08.030.
[93] B. Guo, S.W. Tay, Z.L. Liu, L. Hong, Assimilation of highly porous sulfonated carbon nanospheres into Nafion (R) matrix as proton and water reservoirs, Int. J. Hydrog. Energy 37 (2012) 14482–14491, http://dx.doi.org/10.1016/j.ijhydene.2012.07.112.

Dr. Steven C. DeCaluwe is an Assistant Professor of Mechanical Engineering at the Colorado School of Mines. He received his B.S. in Mathematics and Elementary Education from Vanderbilt University (2000). After teaching elementary school for 3 years, he received a Ph.D. in Mechanical Engineering from the University of Maryland (2009), before serving as a postdoctoral fellow at the NIST Center for Neutron Research (2009–2012). His research employs *in operando* diagnostics and numerical simulation to bridge atomistic and continuum-scale understanding of electrochemical energy devices.

Dr. Andrew Baker is currently a postdoctoral research associate in the Materials Synthesis and Integrated Devices group at Los Alamos National Laboratory. He received his B.S. and Ph.D. in Mechanical Engineering from the University of Delaware. His current research is related to cation transport in PEM fuel cells and PEM fuel cell durability.

Pavan Bhargava received his Bachelors degree from the Electrical Engineering Department at University of Maryland - College Park in 2010. He is currently pursuing his Ph.D. under Professor Vladimir Stojanovic in the Department of Electrical Engineering and Computer Science at the University of California - Berkeley. His research mainly focuses on developing compact and fully integrated LIDAR systems for autonomous vehicles.

John E. Fischer is currently pursuing his Bachelor's degree from the Mechanical Engineering Department at Colorado School of Mines (CSM). He has conducted research at CSM under the supervision of Prof. Steven DeCaluwe since 2014. After graduation in May of 2018, he will join the Process Engineering group at Tesla, Inc., in Fremont, CA. His research interests are energy production and storage technologies, sustainability, polymers, and advanced manufacturing.

Dr. Joseph Dura is a staff scientist at the NIST Center for Neutron Research. He applies Neutron Reflectometry and related techniques to study structures and phenomena in thin-films and interfaces for batteries, fuel cell materials, polymers, hydrogen absorption, magnetism, and biology. He received his B.S. from the University of Arizona and Ph.D. in Physics from the University of Illinois at Urbana-Champaign, and was a postdoc at the University of Houston. He is on the Advisory Board for the International Symposium on Polymer Electrolytes and the Steering committee of CREB, the Center for Research in Extreme Batteries.